Characteristics of airborne black carbon-containing particles during the 2021 summer COVID-19 lockdown in a typical Yangtze River Delta city, China

Yuan Dai[1,2,3], Junfeng Wang[1,2], Houjun Wang[3], Shijie Cui[1,2], Yunjiang Zhang[1,2], Haiwei Li[1,2], Yun Wu[1,2], Ming Wang[1,2], Eleonora Aruffo[5], Xinlei Ge[1,2,4*]

[1]Jiangsu Key Laboratory of Atmospheric Environment Monitoring and Pollution Control, Collaborative Innovation Center of Atmospheric Environment and Equipment Technology, School of Environmental Science and Engineering, Nanjing University of Information Science and Technology, Nanjing 210044, China
[2]International Joint Laboratory on Climate and Environment Change (ILCEC), Nanjing University of Information Science and Technology, 210044 Nanjing, China
[3]Yangzhou Environmental Monitoring Center, Yangzhou 225009, China
[4]School of Environment and Energy Engineering, Anhui Jianzhu University, Hefei 230601, China
[5]Department of Advanced Technologies in Medicine & Dentistry, University "G. d'Annunzio" of Chieti-Pescara; Center for Advanced Studies and Technology-CAST, Chieti 66100, Italy

Correspondence: Xinlei Ge (caxinra@163.com)

Abstract

Black carbon-containing particles (BCc) are ubiquitous in ambient air, significantly contributing to particulate matter (PM) pollution. The unexpected outbreak of the COVID-19 pandemic in the summer of 2021 prompted a localized and prolonged lockdown in Yangzhou City, situated in the Yangtze River Delta, China. This lockdown led to significantly altering in local anthropogenic emissions, while neighboring cities continued regular operations, providing a unique opportunity for the investigation of BCc characteristics influenced by varying emission conditions. Single particle aerosol mass spectrometer (SPA-MS) analysis revealed a notable decrease in the proportion of freshly emitted BCc during the lockdown period (LD). However, $PM_{2.5}$ concentrations remained relatively unchanged, with an observed increase in the proportion of aged BCc during LD compared to the period before the lockdown (BLD). The study also underscored the significant role of regional transport in $PM_{2.5}$ pollution during the campaign. Moreover, reactive trace gases (e.g., NO_x, SO_2, and VOCs) could form thick coatings on pre-existing particles likely via enhanced heterogeneous hydrolysis under high relative humidity (RH) as well, resulting in significant BCc particle growth (~600 nm), as well as $PM_{2.5}$, during LD. Our study highlights that short-term, strict local emission controls may not effectively reduce PM pollution due to the complex production and transmission characteristics of BCc and the non-linear responses of $PM_{2.5}$ to its precursors. Achieving further effective $PM_{2.5}$ reduction mandates a focus on nuanced control of BCc and necessitates a comprehensive and extensive approach with a regionally coordinated and balanced control strategy through joint regulation.

1. Introduction

China has implemented long-term clean air measures to cut down anthropogenic emissions and improve air quality (Ge et al., 2020), resulting in a nationwide reduction of average fine particulate matter (PM$_{2.5}$, aerodynamic diameter $\leq$ 2.5 μm) level from 50 μg m^{-3} in 2015 to 30 μg m^{-3} in 2020 (Zhou et al., 2022). However, this PM$_{2.5}$ concentration remains significantly higher than the new World Health Organization (WHO) guideline value of 5 μg m^{-3} (*WHO Global Air Quality Guidelines*, 2021). Black carbon (BC) is a ubiquitous component of aerosols, typically constituting a small proportion (5~10%) of PM$_{2.5}$ in the atmosphere (Chen et al., 2020). However, freshly emitted BC evolves into BC-containing particles (BCc) by undergoing atmospheric aging, contributing to a rise in the total mass of PM$_{2.5}$ through processes of coating or embedding by other materials (Bond and Bergstrom, 2006; Peng et al., 2016). The number and mass fraction of BCc can excess 60% and 50% of PM$_{2.5}$, respectively, emphasizing the significant role of BC in elevating the mass concentration of particulate matter (PM) (Sun et al., 2022; Xie et al., 2020; Chen et al., 2020).

The atmospheric aging of BCc involves intricate chemical and physical transformations that influence their mixing state, morphology, hygroscopicity, and optical properties, all of which have profound implications for climate and human health (Bond et al., 2013; Ramanathan et al., 2008). For example, freshly emitted BC particles are initially hydrophobic but possess a porous surface structure that facilitates the internal or external mixing with co-emitted primary organic/inorganic and secondary materials that are associated with BC (Cheng et al., 2012; Li et al., 2020). On the other hand, BCc undergoes continually aging processes, including the condensation of low-volatility vapors (Li et al., 2022), coagulation with preexisting aerosols (Kondo et al., 2011), and heterogeneous oxidation with gaseous pollutants (Zhang et al., 2024). This alteration may affect the coating thickness, morphology, size distribution, and hygroscopicity of BCc, thereby impacting their climate forcing as well as atmospheric lifetime (Luo et al., 2022; Taylor et al., 2014). High loading of atmospheric BCc could also depress the development of the planetary boundary layer and exacerbate PM pollution episodes (Huang et al., 2018). BCc characteristics are influenced by various combustion sources and emission conditions, including local industrial burning, vehicle exhausts, residential coal burning, and biomass burning (Li et al., 2020; Sedlacek et al., 2022; Zhang et al., 2018), as well as long-range transport from other regions (Adachi et al., 2014; Zhang et al., 2021). Those diverse conditions complicate the development of parameterizations of BCc properties, the insufficient understanding of complex emission sources, aging processes, and physical properties of BCc, hampering the effectiveness of air quality remediation (Cappa et al., 2019; Kahnert, 2010; Sun et al., 2021).

Studies on the effects of large-scale and short-term stringent emission control events on air quality in China have been widely deployed, e.g., the 2008 Beijing Olympic Games

86 (Wang et al., 2010; Zhou et al., 2010), the 2015 Asia-Pacific Economic Cooperation
87 (APEC) (Zhu et al., 2015), the 2014 Nanjing Youth Olympic Games (Wang et al., 2022)
88 and the national COVID-19 lockdown in 2020 winter (Huang et al., 2021; Le et al.,
89 2020; L. Li et al., 2020; Wang et al., 2020). Previous studies extensively investigated
90 air pollutant variations during the COVID-19 lockdown in the winter of 2020 across
91 different regions of the world. Stringent restrictions on industrial and vehicular
92 activities have resulted in significant reductions in gaseous pollutants and particulate
93 matter, not only in megacities (Chen et al., 2020; Jeong et al., 2022; Sun et al., 2020)
94 but also in middle-sized cities (Clemente et al., 2022; Wang et al., 2021; Xu et al., 2020)
95 and rural areas (Cui et al., 2021, 2020; Jain et al., 2021). Compared to the decreasing
96 trends observed in most cities worldwide, the level of $PM_{2.5}$ in Shanghai (Chang et al.,
97 2020), Hohhot (Zhou et al., 2022), and the Northeast of China Plain (Nie et al., 2021)
98 increased unexpectedly. These observations reveal the complex aerosol chemistry of
99 $PM_{2.5}$ comprising primary and secondary components. The reduction of primary
100 pollutants during lockdown resulted in a shift towards a higher proportion of secondary
101 aerosols, including inorganic and organic species, exhibiting a non-linear response to
102 emission changes (Zhang et al., 2021). Furthermore, some studies suggested that the
103 increase in secondary aerosols during lockdown is due to the enhanced atmospheric
104 oxidative capacity resulting from the rise in ozone levels (Wang et al., 2021),
105 unfavorable meteorological conditions (Chien et al., 2022; Sulaymon et al., 2021a),
106 changes of local and regional emission sources (Feng et al., 2022). However, most
107 previous studies focused on lockdown events during the cold seasons, and studies on
108 summer lockdown events in China were very limited.
109
110 Yangzhou is located in the central region of the Yangtze River Delta (YRD), at the
111 junction of the Yangtze River and, the Beijing-Hangzhou Grand Canal, which serves as
112 a prominent economic city, industrial-intensive area, and highly active inland shipping
113 node in East China. Due to the complex emissions and feedback with the East Asian
114 monsoons (Ding et al., 2019), this region is susceptible to anthropogenic aerosols,
115 especially BCc originating from chemical, steelmaking, coal-fired, petrochemical
116 enterprises, and transportation, etc. Extensive studies have investigated the responses
117 of atmospheric pollutants to emission changes during the COVID-19 lockdown
118 measures in the YRD (Chen et al., 2021; Li et al., 2020; Qin et al., 2021; Zhang et al.,
119 2022). However, the key chemical and physical processes specifically responsible for
120 the BCc in this region are still unclear. During the summer of 2021, Yangzhou
121 experienced a resurgence of COVID-19 with over 500 confirmed cases. In response,
122 stringent public health measures were imposed from July 29th to September 10th,
123 including the closure of public transport, and suspension of non-essential industrial
124 plants, restaurants, shopping malls, and entertainment clubs. People were also
125 mandated to quarantine at home. Consequently, Yangzhou experienced a significant
126 decline in transportation and industrial energy consumption, dropping by nearly 46%
127 and 25%, respectively, compared to the same period in 2020 (www.yangzhou.gov.cn),

128 implying a substantial reduction in human activity and primary emissions. Unlike the
129 nationwide COVID-19 lockdown in China during the cold season of 2020 (Le et al.,
130 2020; Sulaymon et al., 2021b), the summer lockdown in Yangzhou was more localized
131 but protracted, significantly altering local anthropogenic emissions while neighboring
132 cities maintained regular operations, which provides a unique opportunity to explore
133 and compare the diverse mixing states and, the aging process of BCc in different
134 anthropogenic emission conditions in summer. Here we report the chemical
135 compositions and aging characteristics of airborne BCc in YRD. Our investigation
136 involved a combination of ground measurements, spaceborne observations, and mass
137 spectrometric analysis conducted during the COVID-19 lockdown in the summer of
138 2021 in Yangzhou. Additionally, we employed potential source contribution function
139 (PSCF) analysis to investigate the air pollution patterns in the YRD.
140

141 **2. Methods**
142 2.1 Sampling site and instruments
143 The in-situ online measurements were conducted at a rooftop laboratory 20 m above
144 ground located in a national air quality monitoring station, Yangzhou Environmental
145 Monitoring Center (32.41ºN, 119.40ºE), Yangzhou, China (**Figure 1**). This sampling
146 site is a typical urban site surrounded by residential areas, arterial roads, parks,
147 restaurants, and shopping centers. In this study, the measurement period was divided
148 into three phases: the before-lockdown period (BLD: 30 June to 28 July 2021), the
149 lockdown period (LD: 29 July to 9 September 2021), and the after-lockdown period
150 (ALD: 10 September to 7 October 2021) (**Figure 2**).
151

152 A single-particle aerosol mass spectrometer (SPA-MS, Hexin Analytical Instrument Co.,
153 Ltd., China) was deployed during the field campaign to obtain the chemical
154 composition, size distribution, and mixing state of individual $PM_{2.5}$ particles. A cyclone
155 with a 2.5 μm cutpoint (Model URG-2000-30ED) and a Nafion dryer is equipped in
156 front of the sampling inlet. Individual particles are introduced into the SPA-MS through
157 a critical orifice at a flow rate of 3 L min^{-1}. The vacuum aerodynamic diameters (D_{va})
158 are determined using the velocities derived from two continuous laser beams (diode Nd:
159 YAG, 532 nm) spaced 6 cm apart. Subsequently, these particles are desorbed and
160 ionized by a downstream pulsed laser (266 nm), and ion fragments are generated and
161 measured by a Z-shaped bipolar time-of-flight mass spectrometer. A more detailed
162 description of SPA-MS can be found in previous studies (Li et al., 2011).
163

164 $PM_{2.5}$ mass concentration was measured by a particulate matter monitor (XHPM2000E,
165 Xianhe, China). Nitrogen oxides ($NO_x = NO + NO_2$), SO_2, and ozone (O_3)
166 concentrations were detected with a set of Thermo Fisher Scientific instruments
167 (Models 42i, 43i, and 49i). The concentrations of 103 volatile organic compounds
168 (VOCs) in ambient air, comprising 57 ozone precursors (PAMS), 12 aldehydes and
169 ketones, and 34 toxic organics (TO15), were continuously monitored at hourly intervals

using an online device (TH-300B, Tianhong, China). Meteorological parameters, including ambient temperature (T), relative humidity (RH), wind direction (WD), and wind speed (WS) were observed synchronously using an automatic weather instrument (WXT530, Vaisala, Finland). Precipitation (PCP) data was obtained from the Yangzhou Meteorological Bureau. All online data presented in this paper were hourly averaged at local time (Beijing time, UTC+8).

2.2 Data analysis

2.2.1 Satellite Product

In this study, we utilized the Copernicus Atmosphere Monitoring Service (CAMS) Global Near-Real-Time dataset (available at https://developers.google.com/earth-engine/datasets/catalog/ECMWF_CAMS_NRT), acquired from the European Centre for Medium-Range Weather Forecasts (ECMWF), to analyze the distribution of total surface column concentrations of NO_2, SO_2 and surface $PM_{2.5}$ mass concentration. CAMS offers the capacity to continuously monitor the composition of the Earth's atmosphere at global and regional scales since 2016, with a spatial resolution of 44528 meters (Benedetti et al., 2009; Morcrette et al., 2009). The details of the bands of the dataset used in this study are shown in Table S2. We calculated and plotted the averaged 2-dimensional data of ECMWF/CAMS/NRT NO_2, SO_2, and $PM_{2.5}$ during BLD and LD over the region of interest (17.93~54.74 ºN, 71.21~142.23 ºE) using Google Earth Engine (Gorelick et al., 2017). The integration of remote sensing measurements has provided a more comprehensive understanding of the sources and distributions of particle matter and gaseous pollutants facilitating the evaluation of the impact of human activities on air quality.

2.2.2 Geographic Source Analysis

The potential source contribution function (PSCF) analysis, based on the Hybrid Single-Particle Lagrangian Integrated Trajectory (HYSPLIT) model, can be employed to identify regional sources of air pollutants. Before conducting the PSCF analysis, 36 hours of air mass backward trajectories with one-hour resolution at 500 m above ground level were calculated using the wind data from the Global Data Assimilation System (GDAS) provided by the National Oceanic and Atmospheric Administration (NOAA) (Wang et al., 2009). An open-source software MeteoInfo (Wang, 2014) was utilized for the PSCF analysis. The whole study area (110.1~133.4 ºE and 21.3~39.9 ºN) covered by the trajectories was divided into thousands of cells with a spatial resolution of 0.1° × 0.1°. The PSCF was simulated according to the following equation:

$$PSCF_{ij} = \frac{m_{ij}}{n_{ij}} \tag{1}$$

where $PSCF_{ij}$ is the conditional probability that the grid cell (i, j) was a source of the species found in high concentration (Hopke et al., 1993); n_{ij} is the number of all trajectories passing through this grid cell, and m_{ij} is the number of trajectories. In this study, the pollution criterion values for different BCc particle types were set as the 75th

percentile of hourly average number fractions, respectively. To further improve the accuracy of the PSCF analysis and minimize analytical uncertainties, the Weighted PSCF (WPSCF) functions as shown in Equation (2~3) were applied (Polissar et al., 1999). The weight (W_{ij}) for each grid cell was determined based on the number of trajectory endpoints (n_{ij}) as follows:

$$WPSCF_{ij} = W_{ij} \times PSCF_{ij} \tag{2}$$

$$W_{ij} = \begin{cases} 1.00 & n_{ij} > 3n_{ave} \\ 0.70 & 1.5n_{ave} < n_{ij} \leq 3n_{ave} \\ 0.40 & n_{ave} < n_{ij} \leq 1.5n_{ave} \\ 0.17 & n_{ij} \leq n_{ave} \end{cases} \tag{3}$$

Here, n_{ave} is the average number of trajectory endpoints of each grid.

2.2.3 SPA-MS Data Analysis

In total, 1649574 particles were analyzed during the entire observation period. The size and chemical composition of single particles were analyzed using the Computational Continuation Core (COCO V1.4) toolkit in MATLAB 2022 (The MathWorks, Inc.). Our focus was on BCc, which was identified based on the relative peak area (RPA) of carbon ion clusters ($C_n^{\pm}$, n = 1, 2, 3, …), with a threshold of 0.05 (Zhang et al., 2021). An adaptive resonance theory-based neural network algorithm (ART-2a) was applied to classify the measured individual particles based on the presence and intensity of ion peaks, with a vigilance factor of 0.75, a learning rate of 0.05, and 20 iterations (Song et al., 1999).

3. Results and discussion

3.1 Field observations

Figure 2 presents the temporal variations of meteorological parameters, $PM_{2.5}$, NO_x, and SO_2 concentrations. Notably, significantly reductions in $PM_{2.5}$, NO_x, and SO_2 were observed at the end of BLD due to a high precipitation event, with a peak hourly precipitation reaching 37 mm, and the data collected during this event were excluded from the analysis. During BLD, the mean temperature (T) was 28±3 °C, the total precipitation was 221 mm, with an average relative humidity (RH) of 83±12%. The prevailing winds originated from the south and southeast, with a mean wind speed (WS) of 3.3±1.2 m s^{-1}. In comparison, LD shows a decline in temperature to 27±2 °C and WS to 2.3±1.0 m s^{-1}, but an increase in RH to 87±11% and a reduction in total precipitation to 86 mm. **Figure S2b and c** present uniform distributions of RH and boundary-layer height (BLH) across the YRD during LD. These regional meteorological conditions and the effective removal of the pollutants accumulated at the end of BLD facilitated the investigation of BCc regional transport in YRD. During ALD, the temperature declined further to 25±3 °C, WS increased to 3.3±1.5 m s^{-1}, and total precipitation dropped to 27 mm with a lower RH of 77±14%.

247   During LD, strict measures resulted in notably lower surface concentrations of $PM_{2.5}$
248   (20.3 μg m^{-3}), NO_x (16.8 μg m^{-3}) and TVOC (55.9 μg m^{-3}) compared to BLD and ALD.
249   Conversely, the surface O_3 concentration showed an increase of 18.4 μg m^{-3} (28%)
250   during LD relative to BLD. The reduction of fresh NO emission alleviates O_3 titration
251   (Steinfeld, 1998) could be an explanation. Analysis from **Figure S3** indicates that the
252   O_3 level is higher than those of neighboring cities in the YRD, suggesting higher local
253   atmospheric oxidation capacity during LD. However, the average concentrations of
254     $PM_{2.5}$ (20.6 vs. 20.3 μg m^{-3}), SO_2 (9.1 vs. 9.2 μg m^{-3}) and CO (0.61 vs. 0.62 mg m^{-3})
255   were comparable during both BLD and LD (**Figure 3**).After LD, social activities
256   gradually resumed in Yangzhou City, leading to an apparent increase in all observed
257   pollutants during the ALD period. For instance, there were relative increases of 66%
258   for NO_x, 19% for SO_2, 36% for TVOC, 14% for O_3, 32% for $PM_{2.5,}$ and 16% for CO
259   from LD to ALD, respectively (**Figure 3**).

261   Satellite-retrieved $PM_{2.5}$, NO_2, and SO_2 data over the entire region of eastern China
262   were also investigated, and results show that these pollutants were predominantly
263   concentrated in Shanghai and its neighboring cities, including Yangzhou, during both
264   BLD and LD (**Figure S4**). **Figure 4** presents regional fractional changes of mean $PM_{2.5}$,
265   NO_2, and SO_2 concentrations from the BLD to LD periods in YRD, all showing an
266   increase of 29%, 6%, and 14%, respectively. In comparison, Yangzhou city experienced
267   lower increases in these air pollutants, with slight changes of 6%, -18%, and -4% for
268     $PM_{2.5}$, NO_2, and SO_2, respectively. The implication is that, even though local primary
269   emissions, such as NO_2, and SO_2, were reduced substantially during LD, they still could
270   be affected by regional transport. Furthermore, as depicted in **Figure S3**, the
271   concentrations of NO_2 in major cities of the YRD were more than twice higher than in
272   Yangzhou during LD, confirming a relatively lower local primary emissions due to the
273   stringent lockdown. However, the higher level of SO_2 in Yangzhou during LD may be
274   attributed to the nearby power stations along the Yangtze River, which were not
275   impacted by the lockdown measures.

277 ## 3.2 Chemical composition and size distribution of individual BCc
278   Based on the SPA-MS analysis, a total of 1068362 BCc was collected during the whole
279   study period. The BCc accounted for 59%, 69%, and 57% of the total number of
280   measured particles in the BLD, LD, and ALD periods, respectively. **Figure 5** shows the
281   normalized average mass spectra of BCc during three periods. Ion height in each
282   spectrum reflects the number fraction of the detected BCc with the corresponding ion
283   to the total BCc, while colors represent peak area ranges of detected ions. BCc in BLD,
284   LD, and ALD shown similar mass spectra at $m/z < 100$, with common peaks including
285   carbon ion clusters ($C_n^{\pm}$, n = 1~7), m/z 27$[C_2H_3]^+$, 37$[C_3H]^+$, 43$[C_2H_3O]^+$, 51$[C_4H_3]^+$,
286   63$[C_5H_3]^+$, 46$[NO_2]^-$, 62$[NO_3]^-$, and 97$[HSO_4]^-$. However, the abundance of large m/z
287   carbon ions ($C_n^{\pm}$, n > 7) in both BLD and ALD periods was 1.5 times higher than that in
288   the LD. Previous studies have indicated that high-mass carbon ions may be linked to

289 traffic emissions, particularly those from diesel trucks(Xie et al., 2020; Liu et al., 2019),
290 and the observed reduction in such ions during LD suggests a decrease in local vehicle
291 emissions. This trend is also consistent with the changes observed in aromatic
292 compounds, e.g. m/z 119$[C_9H_{11}]^+$.
293
294 Further, BCc was classified into 12 types based on the differences in chemical features
295 and temporal variations, as shown in **Table S1**. Fresh BC particles (BC-fresh) are those
296 freshly emitted without undergoing significant atmospheric processing (Ding et al.,
297 2021). Five types of BC-fresh particles were identified according to their ion markers:
298 (i) BC-pure is dominated by carbon clusters ($C_n^{\pm}$) with minor ion signals of inorganic
299 species, such as m/z 46$[NO_2]^-$ and m/z 97$[HSO_4]^-$ from nitrate and sulfate, respectively
300 (Xie et al., 2020); (ii) BCc from biomass burning (BB) are characterized by ion signals
301 at *m/z* 39$[K]^+$, 45$[CHO_2]^-$, 59$[C_2H_3O_2]^-$, and 73$[C_3H_5O_2]^-$, with a relative peak area
302 (RPA) more than 0.5 (Silva et al., 1999); (iii) coal combustion BCc (CC) typically
303 include small carbon clusters ($C_n^{\pm}$, n = 1~4), metal elements (e.g., m/z 7$[Li]^+$, 23$[Na]^+$,
304 27$[Al]^+$, 56$[Fe]^+$, 63$[Cu]^+$ and 206/207/208$[Pb]^+$), and organic carbon (38$[C_3H_2]^+$,
305 43$[C_2H_3O]^+$) peaks in the positive mass spectrum, while the strong signals of secondary
306 inorganic species (46$[NO_2]^-$, 43$[AlO]^-$, 62$[NO_3]^-$, 80$[SO_3]^-$, 97$[HSO_4]^-$) in the
307 negative ion mode suggest that CC particles were long-distance transported or more
308 processed (Zhang et al., 2022; Zhang et al., 2009); (iv) particles from vehicle emission
309 (VE) are characterized by the presence of ion signals at *m/z* 40$[Ca]^+$, 51$[V]^+$, 55$[Mn]^+$,
310 67$[VO]^+$, 46$[NO_2]^-$, 62$[NO_3]^-$, and 79$[PO_3]^-$, as well as high loadings of organic carbon
311 (41$[C_3H_5]^+$, 43$[C_2H_3O]^+$) and carbon clusters ($C_n^{\pm}$, n = 1~4) ion peaks (Yang et al., 2017);
312 (v) BCc that are internally mixed with more than one type (BB, CC, and VE) are
313 categorized as Mix type (Sun et al., 2022).
314
315 Aged BC particles, denote as BC-aged, undergo a series of chemical reactions and
316 physical transformations. These processes typically lead to changes in their morphology,
317 hygroscopicity, and optical properties as they are coated with other materials (He et al.,
318 2015). Six types of BCc are classified as BC-aged and are further grouped into BCOC
319 and BC-SNA, depending on whether they contain mainly organic carbon (OC) or
320 sulfate/nitrate/ammonium (SNA). First, BCOC types indicate BC-aged particles that
321 are internally mixed with OC. These particles are characterized by the presence of
322 carbon clusters ($C_n^{\pm}$) and $C_nH_m^+$ ions (n = 1~6, m = 1~3) in positive mass spectra (Xie
323 et al., 2020). On the other hand, BC-aged particles that do not mix with OC are named
324 BC-SNA indicating the mix with secondary inorganic species. Additionally, BCOC
325 particles with negative mass spectra dominated by nitrate ions (46$[NO_2]^-$ and 62$[NO_3]^-$)
326 or sulfate ions (97$[HSO_4]^-$) are referred to as BCOC-N or BCOC-S, respectively;
327 otherwise, BCOC particles showing similar peak areas of nitrate and sulfate are named
328 BCOC-SN. The BC-SNA particles are further categorized as BC-N, BC-S, and BC-SN
329 based on similar principles. Note the remaining particles that cannot be classified into
330 either BC-fresh or BC-aged ones are denoted as BC-other. More details of BCc particle

331 types are shown in **Table S1** and **Figure S1** in the Supplement.

332

333 During BLD, the average number fraction of BC-fresh particles was 36% with sizes
334 mainly concentrated at 500 nm, similar to the mode size of BC-aged particles was 520
335 nm (**Figures 6**). The predominant BCc types during BLD were BCOC-S and BC-S (24%
336 and 12% by number), likely because sulfate was removed less efficiently than organic
337 matter (OM) and NO_3 by heavy precipitation, especially during the warm seasons
338 (Isokääntä et al., 2022). As shown in **Figures 6c and d**, the peak size of BC-SNA was
339 larger than that of BCOC in all periods, indicating that organics coated BCc generally
340 had a relatively thin coating compared to those coated by secondary inorganic species,
341 which is consistent with previous studies (Sun et al., 2016; Wang et al., 2019).

342

343 During the transition from BLD to LD, heavy and continuous precipitation occurred
344 from July 25th to July 28th (the eve of lockdown), resulting in the removal of a majority
345 of the pollutants ($PM_{2.5}$: 4 μg m^{-3}, O_3: 35 μg m^{-3}, NO_x: 8 μg m^{-3}). Following this
346 environmental clearance, strict lockdown measures were implemented, resulting in a
347 drastic reduction in primary emissions. As a result, the number fraction of BC-fresh
348 particles significantly decreased from 37% to 28% and that of VE-type particles
349 dropped from 12% to 3% (by number). Expectedly, with the decrease in NO_x, an
350 obvious enhancement of O_3 was observed during LD (**Figure 3**). According to previous
351 studies (Huang et al., 2021; Laughner et al., 2021), large reduction of NO_x may promote
352 the formation of O_3 under a VOC-limited regime and enhance the oxidation capacity of
353 the local atmosphere, which may promote the number fraction of BC-aged particles
354 increased from 64% in the BLD to 72% in LD (**Figure 7a**), indicating the lockdown
355 could accelerate aging of BCc through complicated chemical reactions and/or physical
356 coagulation. Additionally, the most abundant type of BCc changed from BCOC-S (24%
357 by number) in the BLD to BC-N (25%) in LD (**Figure 7a**), suggesting different BCc
358 formation pathways. Despite the abrupt reductions of NO_x (-39%) due to the city
359 lockdown, it is important to note that the concentration of $PM_{2.5}$ only slightly decreased
360 during LD (-1%), highlighting the non-linear relationship between primary emissions
361 and $PM_{2.5}$ levels.

362

363 During ALD ($PM_{2.5}$: 26.7 μg m^{-3}, NO_x: 27.9 μg m^{-3}, TVOC: 76.0 μg m^{-3}), the number
364 fraction of BC-fresh particles rose from 28% (LD) to 31% (ALD), while the fraction of
365 VE particles also increased from 3% (LD) to 12% (ALD) (**Figure 7a),** coinciding with
366 a 16% rise in CO concentration. This suggests a shift in combustion practices and fuel
367 usage patterns as economic activities resumed. The increased CO levels, a known
368 marker for combustion-related emissions, align with the resurgence of vehicle
369 emissions and other activities that emit BC and CO concurrently (Wang et al., 2015,
370 Zhou et al., 2009). Notably, the size distributions of BC-fresh and BC-aged particles
371 presented relatively small peaks at 690 nm and 820 nm during ALD, in addition to the
372 prominent peaks at 490 nm and 500 nm, which were different from those in the BLD

373   and LD periods. These small peaks were relatively close to the dominant sizes of BC-
374   fresh and BC-aged particles during LD (**Figure 6**). This result suggests that a substantial
375   number of BCc with small sizes (around 500 nm) after the lockdown was lifted in
376   Yangzhou, owing to the sudden enhancement of primary emissions; on the other hand,
377   particles with large diameters (>690 nm) may have formed due to the participation of
378   more trace reactive gases (e.g., NO_x, SO_2, and VOCs) in continuous aging reactions,
379   resulting in thicker coatings on the surface of pre-existing particles and therefore a more
380   clear separation of two-mode sizes during the ALD period than during the other two
381   periods. This hypothesis was also supported by the increased number fraction of
382   BCOC-SN during the ALD period (**Figure 7a**). Similar findings have been reported in
383   the North China Plain (NCP) and the YRD during cold seasons, where thicker coatings
384   on secondary aerosols were also observed under lower RH (<70%) (Zhang et al., 2021).
385   This might be due to that particles with more organics and nitrate can result in earlier
386   deliquescence and provide aqueous surfaces that facilitate the heterogeneous formation
387   of secondary species under relatively low RH (Zhang et al., 2021). Among the three
388   periods, the difference between the mode sizes of BC-aged and BC-fresh particles was
389   the smallest (10 nm) during the ALD period (**Figure 6a and b**). This size reduction can
390   be attributed to the increased BCOC and hydrophobic primary particles after lockdown
391   (Figure 7). Because the internally mixed BCOC and hydrophobic primary particles may
392   constrain further growth of secondary BC-SNA particles (Liu et al., 2016; Zhang et al.,
393   2018), thereby leading to smaller-sized BC-aged particles. Moreover, the differences in
394   BCc mode sizes between ALD and BLD periods also reveal an interesting fact that the
395   lockdown effect may not only affect air quality during lockdown but also can influence
396   the air quality even after lockdown, as the resumed emissions after lockdown may be
397   subjected to different chemistry from that before lockdown.
398
399   Throughout the entire observation, the changes in the number fraction of BC-SNA
400   exhibited consistency with the variations in RH (**Figure 7b**), indicating that BC tends
401   to mix with ammonium sulfate and ammonium nitrate under high RH conditions.
402   Meanwhile, the number fraction of BCOC shows similar patterns as TVOC, suggesting
403   that high TVOC levels may facilitate the coating of organics on BC cores under low
404   RH condition. **Figure 8** displays the number fraction of BCc species as a function of
405    $PM_{2.5}$. Overall, as $PM_{2.5}$ levels increased, the number fraction of BC-aged particles also
406   increased, while the proportion of BC-fresh particles decreased during BLD and LD,
407   indicating a clear transition from BC-fresh particles to more aged ones, in line with the
408   average size distribution during ALD has a small peak at 900 nm. Specifically, the
409   increase in $PM_{2.5}$ was driven by BCOC-S during BLD (**Figure 8a**), whereas BC-N
410   played a vital role in the $PM_{2.5}$ increase during LD (**Figure 8b**). Interestingly, the
411   concentration of NO_x, the primary precursor of BC-N, decreased by 31% and 41%
412   during LD compared to BLD and ALD, respectively (**Figure 3**), indicating a strong
413   non-linear response of nitrate in BCc to NO_x, likely due to much faster conversion of
414   NO_x to nitrate upon enhanced atmospheric oxidation capacity; additionally, the high

415   proportion of BC-N during LD might be attributed to regional transport, similar to that
416   in Shanghai during 2020 winter lockdown (Chang et al., 2020).

417

418   ## 3.3 Chemical aging of BCc

419   As shown in **Figure 5**, in the average positive mass spectra of total BCc, the peak areas
420   of C_n^+, OM, and metals contributed to more than 95% of the total, while nitrate and
421   sulfate peak areas accounted for more than 90% of the negative mass spectral signal.
422   To better elucidate the aging processes of BCc during different lockdown periods, we
423   summed the carbon clusters $C_n^\pm$ (n = 1~5, accounting for more than 99% of C_n) peak
424   areas to represent BC, and the total peak area of sulfate, nitrate, and ammonium (SNA)
425   to represent the second inorganic components coated on BC. Additionally, we defined
426   the sum of positive peak areas, excluding C_n^+ and metals, as OC to represent the OM
427   coated on BC. These peak areas encompassed almost all the coating materials, except
428   for metals, of BCc. The changes in the mixing state and morphology of BCc can provide
429   insights into their aging characteristics, as reported previously (Kandler et al., 2018;
430   Moffet et al., 2013). In this study, we use OC/C_n and SNA/C_n ratios to describe different
431   types of chemical components coated on BC-fresh, and we use the ratio of the mode
432   size of BC-aged (D_{aged}) to that of contemporaneous BC-fresh (D_{fresh}) to represent the
433   aging degree of BCc.

434

435   **Figure 9** illustrates the diurnal variations of the OC/C_n and SNA/C_n ratios along with
436   the size distribution of BCc during different periods. We observed that both OC/C_n and
437   SNA/C_n increased during nighttime and decreased during daytime. These variations
438   showed the prominent enhancements of nocturnal OM and SNA, which could be
439   attributed to the accelerated gas-to-particle partitioning and nocturnal secondary
440   formation of organic/inorganic components under high relative humidity (RH > 85%)
441   and relatively stagnant air mass (WS < 3 m s^{-1}) (**Figure S5**). It is worth noting that from
442   BLD to LD and ALD, the intensity of diurnal variations of OC/C_n and SNA/C_n
443   increased obviously. This discrepancy can be attributed to several reasons. (i) During
444   BLD, the frequent precipitations effectively scavenged the particles (Isokääntä et al.,
445   2022); (ii) In contrast, stronger solar radiation and higher O_3 concentration during LD
446   promoted photochemical formations of OC and SNA; (iii) After lockdown, more
447   precursors due to increased local emissions may lead to more production of secondary
448   components than that during BLD as explained earlier. These results indicate that the
449   aging process and mixing state of BCc depend strongly on meteorological conditions
450   as well as emission sources in urban cities.

451

452   As shown in **Figure 9**, BCc with ~400 nm D_{va} exhibited significant diurnal fluctuations
453   in the OC/C_n and SNA/C_n ratios, during LD. There is a noticeable increase in the
454   proportion of BC-SNA particles during nighttime when RH is relatively high. These
455   observations suggest that nighttime heterogeneous hydrolysis may be considered a key
456   mechanism responsible for the formation of BCOC and BC-SNA particles. According

to Jacobson (2002), coagulation can be significant between particles with sizes <100nm and >1μm but insignificant for particles of >300nm, when the total particle number concentration is higher than 10^4 cm^{-3}. During LD, the OC/C_n and SNA/C_n ratios of BCc with ~400 nm D_{va} exhibited pronounced diurnal variations (**Figure 9**) and the number fraction of BC-SNA increased obviously. Despite the difference between D_{va} and physical diameter, such results imply that chemical reactions should be considered as the major pathway for BCOC and BC-SNA particles of ~400 nm D_{va}, while the large-sized BC-aged particles (>1 μm) may be partially from physical coagulation. The more significant diurnal fluctuations in the OC/Cn and SNA/Cn ratios of BCc particles during the ALD period, compared to the LD period, can be attributed to increased primary emissions from resumed society activities, more complex atmospheric chemistry involving reactive gases, and the reinstatement of typical diurnal emission patterns, with higher nighttime RH further enhancing secondary aerosol formation.

According to Surdu et al. (2023), condensation involves the direct deposition of gas-phase molecules onto the surface of particles, driven by the difference between the condensable gases concentration (C_g) and its equilibrium particle-phase concentration (C_{eq}), which is negatively affected by RH. In our study, the average RH was relatively high during all three periods (>75%), but the condensable vapor concentration decreased during the lockdown period due to strict lockdown measures, making the difference between C_g and C_{eq} smaller during LD compared to the other two periods. Additionally, we observed a larger mode peak (600 nm, Dva) and higher Daged/Dfresh ratios (1.11) compared to BLD (510 nm, 1.03) and ALD (500 nm, 1.02) (**Figure 6**). Therefore, we conclude that condensation was likely inhibited during the LD period. Instead, the conditions likely favored aqueous-phase and heterogeneous reactions, which played a more important role in the evident growth of BCc particles, converting partially coated particles into fully thickly coated BCc during the LD period.

3.4 Source apportionment of BCc during lockdown

In addition to local emissions, regional transport plays a significant role in influencing pollutant levels. The emergent lockdown in Yangzhou led to strict limitation on local emissions, while surrounding cities were still running as usual. This is supported by **Figure S6**, which illustrates the PM$_{2.5}$ concentrations in Yangzhou and the other five surrounding YRD cities (e.g., Nanjing, Zhenjiang, Changzhou, Taizhou, and Chuzhou) during the campaign. High correlations between PM$_{2.5}$ concentrations in Yangzhou and the other five cities were observed across all different periods (**Figure S6**). These findings underscore the importance of the regional transport in PM$_{2.5}$ pollution during the campaign, providing a unique opportunity to investigate the transmission and source characteristics of BCc in YRD during summer. Herein, PSCF analysis was applied to qualitatively simulate the source probability distributions of the specific BCc particle types (BC-fresh, BC-aged, BCOC, and BC-SNA) during LD.

499 As shown in **Figure 10**, the hotspots of potential sources for the four particle types
500 exhibited strong agreements with each other and primarily concentrated in the southeast
501 of Yangzhou, especially along the coast of the Yangtze River, with the WPSCF greater
502 than 0.6. These hotspot areas also encompassed chemical enterprises, power plants,
503 petrochemical industrial parks, and the Yangtze River in the YRD. This evidence
504 suggests that the region of southeast Yangzhou and lower reaches of the Yangtze River
505 are major source areas for the regionally transported BCc in Yangzhou during lockdown.
506 Additionally, Luo et al. (2023) reported that regional transport of pollutants can occur
507 near the surface from upwind areas when the wind speed (WS) exceeds 2 m s^{-1}. **Figure**
508 **S5b** shows that the mean daytime WS was 3 m s^{-1}, indicating that both BC-fresh and
509 BC-aged particles, along with trace gases (e.g., SO_2, NO_x, and VOCs), originating from
510 the hotspot areas, could be transported effectively to Yangzhou. Additionally, the
511 average size of BCc remained around 600 nm at daytime (**Figure S5c**), suggesting that
512 BCc could undergo continual aging reactions under relatively lower RH, but produce
513 relatively thinly coated BCc with smaller sizes than those at nighttime (average size of
514 650 nm). The mean nocturnal WS decreased to 2 m s^{-1}, indicating that the regional
515 atmosphere becomes stagnant (**Figures S5a, b**). As mentioned earlier and underscored
516 here again, this stagnant and humid atmospheric condition may promote aqueous or
517 heterogeneous reactions, likely further leading to the production of more thickly coated
518 BCc than daytime ones.
519
520 ## 4. Conclusions and implications
521 During the summer of 2021, the COVID-19 lockdown imposed in Yangzhou resulted
522 in a significant decrease in anthropogenic emissions from traffic and manufacturing
523 sectors. To examine the effects of this lockdown, we utilized spaceborne observations,
524 ground-based measurements, and particularly SPA-MS analysis to explore the
525 variations, aging characteristics, and sources of BCc in the YRD. We showed that the
526 strict emission controls effectively reduced local gaseous pollutants. However, the
527 decline in NO_x (-39%) and TVOC (-14%) levels might on the other hand result in
528 increased O_3 (28%), leading to a rise in BC-aged particles and a slight elevation in $PM_{2.5}$
529 levels during the lockdown. Our results revealed a strong non-linear response of $PM_{2.5}$
530 and O_3 to the gaseous precursors.
531
532 The SPA-MS analysis results further demonstrate significant enhancement of OM and
533 SNA coating species on BC-fresh particles, owing to gas-to-particle partitioning and
534 nocturnal multiphase chemistry. Consequently, we observed a higher fraction of BC-
535 aged particles (73%) during the lockdown due to enhanced oxidizing capacity and high
536 relative humidity (RH > 85%). The BC-fresh particles tended to mix with SNA under
537 high RH conditions, while high TVOC levels were accompanied by BCOC formation.
538 However, BCOC particles generally exhibited smaller sizes compared to BC-SNA
539 particles. Moreover, we propose that aqueous or heterogeneous reactions might be
540 important to generate BCOC and BC-SNA particles, especially ones with 400 nm D_{va},

541   while coagulation might play a more prominent role in larger BC-aged particles. The
542   aging process during LD promoted the conversion of partly coated particles to totally
543   coated ones, with larger diameters (600 nm) and thicker coatings.
544
545   It should be noted that the observed average $PM_{2.5}$ concentration during the lockdown
546   in Yangzhou was 20 μg m^{-3}, which still significantly exceeds the WHO's air quality
547   guideline of 5 μg m^{-3}. Our research underscores the crucial role of BCc, which
548   constitutes a significant portion of $PM_{2.5}$, in particulate matter pollution. These particles
549   originate from diverse combustion sources and their behavior is intricately influenced
550   by complex chemistry, regional transport, and meteorological factors. Mere reductions
551   in local primary emissions from traffic and manufacturing sectors exhibit limited
552   efficacy in air quality improvement. Therefore, effective air quality remediation
553   strategies necessitate nuanced control of BCc alongside broader emission reduction
554   efforts. We suggest a more comprehensive regulation of precursor gases from multiple
555   sectors, a wide-ranging joint regulation approach as well as proper consideration of the
556   chemistry, to develop an effective strategy for air quality improvement.

Data availability. The data in this study are available from the corresponding author upon request (caxinra@163.com).

Author contributions. XG, JW, and YD designed the research. YD, HW, and SC conducted the field measurements. YD, HW, JW, and SC analyzed the data. XG, JW, HL, YW, YZ, and EA reviewed the paper and provided useful suggestions. YD, JW, and XG wrote the first draft of the paper. All people were involved in the discussion of the results.

Supplement. The supplement related to this article is available online at XXX.

Competing interests. The contact author has declared that neither they nor their co-authors have any competing interests.

Financial support. This research has been supported by the National Natural Science Foundation of China (grant nos. 42377100, 22276099, and 42021004).

References

Adachi, K., Zaizen, Y., Kajino, M., Igarashi, Y., 2014. Mixing state of regionally transported soot particles and the coating effect on their size and shape at a mountain site in Japan. Journal of Geophysical Research: Atmospheres 119, 5386–5396. https://doi.org/10.1002/2013JD020880

Benedetti, A., Morcrette, J.-J., Boucher, O., Dethof, A., Engelen, R.J., Fisher, M., Flentje, H., Huneeus, N., Jones, L., Kaiser, J.W., Kinne, S., Mangold, A., Razinger, M., Simmons, A.J., Suttie, M., 2009. Aerosol analysis and forecast in the European Centre for Medium-Range Weather Forecasts Integrated Forecast System: 2. Data assimilation. Journal of Geophysical Research: Atmospheres 114. https://doi.org/10.1029/2008JD011115

Bond, T.C., Bergstrom, R.W., 2006. Light Absorption by Carbonaceous Particles: An Investigative Review. Aerosol Science and Technology 40, 27–67. https://doi.org/10.1080/02786820500421521

Bond, T.C., Doherty, S., Fahey, D.W., Forster, P., Berntsen, T., DeAngelo, B., Flanner, M., Ghan, S., Kärcher, B., Koch, D., Kinne, S., Kondo, Y., Quinn, P.K., Sarofim, M., Schultz, M., Michael, S., Venkataraman, C., Zhang, H., Zhang, S., Zender, C.S., 2013. Bounding the role of black carbon in the climate system: A Scientific assessment. Journal of Geophysical Research: Atmospheres 118, 5380–5552. https://doi.org/10.1002/jgrd.50171

Cappa, C.D., Zhang, X., Russell, L.M., Collier, S., Lee, A.K.Y., Chen, C.-L., Betha, R., Chen, S., Liu, J., Price, D.J., Sanchez, K.J., McMeeking, G.R., Williams, L.R., Onasch, T.B., Worsnop, D.R., Abbatt, J., Zhang, Q., 2019. Light Absorption by Ambient Black and Brown Carbon and its Dependence on Black Carbon Coating State for Two California, USA, Cities in Winter and Summer. Journal of Geophysical Research: Atmospheres 124, 1550–1577. https://doi.org/10.1029/2018JD029501

Chang, Y., Huang, R., Ge, X., Huang, X., Hu, J., Duan, Y., Zou, Z., Liu, X., Lehmann, M.F., 2020. Puzzling Haze Events in China During the Coronavirus (COVID-19) Shutdown. Geophys. Res. Lett. 47. https://doi.org/10.1029/2020GL088533

Chen, H., Huo, J., Fu, Q., Duan, Y., Xiao, H., Chen, J., 2020. Impact of quarantine measures on chemical compositions of PM2.5 during the COVID-19 epidemic in Shanghai, China. Science of The Total Environment 743, 140758. https://doi.org/10.1016/j.scitotenv.2020.140758

Chen, L., Qi, X., Nie, W., Wang, J., Xu, Zheng, Wang, T., Liu, Y., Shen, Y., Xu, Zhengning, Kokkonen, T., Chi, X., Aalto, P., Paasonen, P., Kerminen, V.-M., Petäjä, T., Kulmala, M., Ding, A., 2021. Cluster Analysis of Submicron Particle Number Size Distributions at the SORPES Station in the Yangtze River Delta of East China. Journal of Geophysical Research: Atmospheres 126. https://doi.org/10.1029/2020JD034004

Chen, L., Zhang, F., Yan, P., Wang, X., Sun, L., Li, Y., Zhang, X., Sun, Y., Li, Z., 2020. The large proportion of black carbon (BC)-containing aerosols in the urban

atmosphere. Environmental Pollution 263, 114507. https://doi.org/10.1016/j.envpol.2020.114507

Cheng, Y.F., Su, H., Rose, D., Gunthe, S.S., Berghof, M., Wehner, B., Achtert, P., Nowak, A., Takegawa, N., Kondo, Y., Shiraiwa, M., Gong, Y.G., Shao, M., Hu, M., Zhu, T., Zhang, Y.H., Carmichael, G.R., Wiedensohler, A., Andreae, M.O., Pöschl, U., 2012. Size-resolved measurement of the mixing state of soot in the megacity Beijing, China: diurnal cycle, aging and parameterization. Atmospheric Chemistry and Physics 12, 4477–4491. https://doi.org/10.5194/acp-12-4477-2012

Chien, L.-C., Chen, L.-W.A., Lin, R.-T., 2022. Lagged meteorological impacts on COVID-19 incidence among high-risk counties in the United States—a spatiotemporal analysis. J Expo Sci Environ Epidemiol 32, 774–781. https://doi.org/10.1038/s41370-021-00356-y

Clemente, Á., Yubero, E., Nicolás, J.F., Caballero, S., Crespo, J., Galindo, N., 2022. Changes in the concentration and composition of urban aerosols during the COVID-19 lockdown. Environmental Research 203, 111788. https://doi.org/10.1016/j.envres.2021.111788

Cui, S., Xian, J., Shen, F., Zhang, L., Deng, B., Zhang, Y., Ge, X., 2021. One-Year Real-Time Measurement of Black Carbon in the Rural Area of Qingdao, Northeastern China: Seasonal Variations, Meteorological Effects, and the COVID-19 Case Analysis. Atmosphere 12, 394. https://doi.org/10.3390/atmos12030394

Cui, Y., Ji, D., Maenhaut, W., Gao, W., Zhang, R., Wang, Y., 2020. Levels and sources of hourly PM2.5-related elements during the control period of the COVID-19 pandemic at a rural site between Beijing and Tianjin. Science of The Total Environment 744, 140840. https://doi.org/10.1016/j.scitotenv.2020.140840

Ding, A., Huang, X., Nie, W., Chi, X., Xu, Zheng, Zheng, L., Xu, Zhengning, Xie, Y., Qi, X., Shen, Y., Sun, P., Wang, J., Wang, L., Sun, J., Yang, X.-Q., Qin, W., Zhang, X., Cheng, W., Liu, W., Pan, L., Fu, C., 2019. Significant reduction of PM$_{2.5}$ in eastern China due to regional-scale emission control: evidence from SORPES in 2011–2018. Atmospheric Chemistry and Physics 19, 11791–11801. https://doi.org/10.5194/acp-19-11791-2019

Ding, S., Liu, D., Hu, K., Zhao, D., Tian, P., Wang, F., Li, R., Chen, Y., He, H., Huang, M., Ding, D., 2021. Optical and hygroscopic properties of black carbon influenced by particle microphysics at the top of the anthropogenically polluted boundary layer. Atmospheric Chemistry & Physics 21, 681–694. https://doi.org/10.5194/acp-21-681-2021

Feng, Z., Zheng, F., Liu, Y., Fan, X., Yan, C., Zhang, Y., Daellenbach, K.R., Bianchi, F., Petäjä, T., Kulmala, M., Bao, X., 2022. Evolution of organic carbon during COVID-19 lockdown period: Possible contribution of nocturnal chemistry. Sci Total Environ 808, 152191. https://doi.org/10.1016/j.scitotenv.2021.152191

Ge, B., Xu, D., Wild, O., Yao, X., Wang, J., Chen, X., Qixin, T., Pan, X., Wang, Z., 2020. Inter-annual variations of wet deposition in Beijing during 2014–2017:

implications of below-cloud scavenging of inorganic aerosols. https://doi.org/10.5194/acp-2020-1146

Gorelick, N., Hancher, M., Dixon, M., Ilyushchenko, S., Thau, D., Moore, R., 2017. Google Earth Engine: Planetary-scale geospatial analysis for everyone. Remote Sensing of Environment, Big Remotely Sensed Data: tools, applications and experiences 202, 18–27. https://doi.org/10.1016/j.rse.2017.06.031

He, C., Liou, K.-N., Takano, Y., Zhang, R., Levy Zamora, M., Yang, P., Li, Q., Leung, L.R., 2015. Variation of the radiative properties during black carbon aging: theoretical and experimental intercomparison. Atmospheric Chemistry and Physics 15, 11967–11980. https://doi.org/10.5194/acp-15-11967-2015

Hopke, P.K., Gao, N., Cheng, M.-D., 1993. Combining chemical and meteorological data to infer source areas of airborne pollutants. Chemometrics and Intelligent Laboratory Systems, Proceedings of the 5th Conference on Computer Applications in Analytical Chemistry (COMPANA '92) 19, 187–199. https://doi.org/10.1016/0169-7439(93)80103-O

Huang, X., Ding, A., Gao, J., Zheng, B., Zhou, D., Qi, X., Tang, R., Wang, J., Ren, C., Nie, W., Chi, X., Xu, Z., Chen, L., Li, Y., Che, F., Pang, N., Wang, H., Tong, D., Qin, W., Cheng, W., Liu, W., Fu, Q., Liu, B., Chai, F., Davis, S.J., Zhang, Q., He, K., 2021. Enhanced secondary pollution offset reduction of primary emissions during COVID-19 lockdown in China. Natl Sci Rev 8, nwaa137. https://doi.org/10.1093/nsr/nwaa137

Huang, X., Wang, Z., Ding, A., 2018. Impact of Aerosol-PBL Interaction on Haze Pollution: Multiyear Observational Evidences in North China. Geophysical Research Letters 45, 8596–8603. https://doi.org/10.1029/2018GL079239

Isokääntä, S., Kim, P., Mikkonen, S., Kühn, T., Kokkola, H., Yli-Juuti, T., Heikkinen, L., Luoma, K., Petäjä, T., Kipling, Z., Partridge, D., Virtanen, A., 2022. The effect of clouds and precipitation on the aerosol concentrations and composition in a boreal forest environment. Atmospheric Chemistry and Physics 22, 11823–11843. https://doi.org/10.5194/acp-22-11823-2022

Jacobson, M.Z., 2002. Analysis of aerosol interactions with numerical techniques for solving coagulation, nucleation, condensation, dissolution, and reversible chemistry among multiple size distributions. Journal of Geophysical Research: Atmospheres 107, AAC 2-1-AAC 2-23. https://doi.org/10.1029/2001JD002044

Jain, C.D., Madhavan, B.L., Singh, V., Prasad, P., Sai Krishnaveni, A., Ravi Kiran, V., Venkat Ratnam, M., 2021. Phase-wise analysis of the COVID-19 lockdown impact on aerosol, radiation and trace gases and associated chemistry in a tropical rural environment. Environmental Research 194, 110665. https://doi.org/10.1016/j.envres.2020.110665

Jeong, C.-H., Yousif, M., Evans, G.J., 2022. Impact of the COVID-19 lockdown on the chemical composition and sources of urban PM2.5. Environmental Pollution 292, 118417. https://doi.org/10.1016/j.envpol.2021.118417

Kahnert, M., 2010. On the Discrepancy between Modeled and Measured Mass

Absorption Cross Sections of Light Absorbing Carbon Aerosols. Aerosol Science and Technology 44, 453–460. https://doi.org/10.1080/02786821003733834

Kandler, K., Schneiders, K., Ebert, M., Hartmann, M., Weinbruch, S., Prass, M., Pöhlker, C., 2018. Composition and mixing state of atmospheric aerosols determined by electron microscopy: method development and application to aged Saharan dust deposition in the Caribbean boundary layer. Atmospheric Chemistry and Physics 18, 13429–13455. https://doi.org/10.5194/acp-18-13429-2018

Kondo, Y., Matsui, H., Moteki, N., Sahu, L., Takegawa, N., Kajino, M., Zhao, Y., Cubison, M.J., Jimenez, J.L., Vay, S., Diskin, G.S., Anderson, B., Wisthaler, A., Mikoviny, T., Fuelberg, H.E., Blake, D.R., Huey, G., Weinheimer, A.J., Knapp, D.J., Brune, W.H., 2011. Emissions of black carbon, organic, and inorganic aerosols from biomass burning in North America and Asia in 2008. Journal of Geophysical Research: Atmospheres 116. https://doi.org/10.1029/2010JD015152

Laughner, J.L., Neu, J.L., Schimel, D., Wennberg, P.O., Barsanti, K., Bowman, K.W., Chatterjee, A., Croes, B.E., Fitzmaurice, H.L., Henze, D.K., Kim, J., Kort, E.A., Liu, Z., Miyazaki, K., Turner, A.J., Anenberg, S., Avise, J., Cao, H., Crisp, D., de Gouw, J., Eldering, A., Fyfe, J.C., Goldberg, D.L., Gurney, K.R., Hasheminassab, S., Hopkins, F., Ivey, C.E., Jones, D.B.A., Liu, J., Lovenduski, N.S., Martin, R.V., McKinley, G.A., Ott, L., Poulter, B., Ru, M., Sander, S.P., Swart, N., Yung, Y.L., Zeng, Z.-C., 2021. Societal shifts due to COVID-19 reveal large-scale complexities and feedbacks between atmospheric chemistry and climate change. Proc Natl Acad Sci U S A 118, e2109481118. https://doi.org/10.1073/pnas.2109481118

Le, T., Wang, Y., Liu, L., Yang, J., Yung, Y.L., Li, G., Seinfeld, J.H., 2020. Unexpected air pollution with marked emission reductions during the COVID-19 outbreak in China. Science 369, 702–706. https://doi.org/10.1126/science.abb7431

Li, J., Jiang, L., Chen, C., Liu, D., Du, S., Zhang, Y., Yang, Y., Tang, L., 2020. Characteristics and Sources of Black Carbon Aerosol in a Mega-City in the Western Yangtze River Delta, China. Atmosphere 11, 315. https://doi.org/10.3390/atmos11040315

Li, K., Wang, X., Lu, X., Chen, H., Yang, X., 2022. Effects of Volatile Components on Mixing State and Size Distribution of Individual Black Carbon Aerosols. Aerosol Air Qual. Res. 22, 210400. https://doi.org/10.4209/aaqr.210400

Li, L., Huang, Z., Dong, J., Li, M., Gao, W., Nian, H., Fu, Z., Zhang, G., Bi, X., Cheng, P., Zhou, Z., 2011. Real time bipolar time-of-flight mass spectrometer for analyzing single aerosol particles. International Journal of Mass Spectrometry 303, 118–124. https://doi.org/10.1016/j.ijms.2011.01.017

Li, L., Li, Q., Huang, L., Wang, Q., Zhu, A., Xu, J., Liu, Ziyi, Li, H., Shi, L., Li, R., Azari, M., Wang, Y., Zhang, X., Liu, Zhiqiang, Zhu, Y., Zhang, K., Xue, S., Ooi,

741   M.C.G., Zhang, D., Chan, A., 2020. Air quality changes during the COVID-19

742   lockdown over the Yangtze River Delta Region: An insight into the impact of

743   human activity pattern changes on air pollution variation. Science of The Total

744   Environment 732, 139282. https://doi.org/10.1016/j.scitotenv.2020.139282

745   Liu, D., Joshi, R., Wang, J., Yu, C., Allan, J.D., Coe, H., Flynn, M.J., Xie, C., Lee, J.,

746   Squires, F., Kotthaus, S., Grimmond, S., Ge, X., Sun, Y., Fu, P., 2019.

747   Contrasting physical properties of black carbon in urban Beijing between winter

748   and summer. Atmospheric Chemistry and Physics 19, 6749–6769.

749   https://doi.org/10.5194/acp-19-6749-2019

750   Liu, Q., Jing, B., Peng, C., Tong, S., Wang, W., Ge, M., 2016. Hygroscopicity of

751   internally mixed multi-component aerosol particles of atmospheric relevance.

752   Atmospheric Environment 125, 69–77.

753   https://doi.org/10.1016/j.atmosenv.2015.11.003

754   Luo, J., Li, Z., Zhang, C., Zhang, Q., Zhang, Yongming, Zhang, Ying, Curci, G.,

755   Chakrabarty, R.K., 2022. Regional impacts of black carbon morphologies on

756   shortwave aerosol–radiation interactions: a comparative study between the US

757   and China. Atmospheric Chemistry and Physics 22, 7647–7666.

758   https://doi.org/10.5194/acp-22-7647-2022

759   Moffet, R.C., Rödel, T.C., Kelly, S.T., Yu, X.Y., Carroll, G.T., Fast, J., Zaveri, R.A.,

760   Laskin, A., Gilles, M.K., 2013. Spectro-microscopic measurements of

761   carbonaceous aerosol aging in Central California. Atmospheric Chemistry and

762   Physics 13, 10445–10459. https://doi.org/10.5194/acp-13-10445-2013

763   Morcrette, J.-J., Boucher, O., Jones, L., Salmond, D., Bechtold, P., Beljaars, A.,

764   Benedetti, A., Bonet, A., Kaiser, J.W., Razinger, M., Schulz, M., Serrar, S.,

765   Simmons, A.J., Sofiev, M., Suttie, M., Tompkins, A.M., Untch, A., 2009.

766   Aerosol analysis and forecast in the European Centre for Medium-Range

767   Weather Forecasts Integrated Forecast System: Forward modeling. Journal of

768   Geophysical Research: Atmospheres 114.

769   https://doi.org/10.1029/2008JD011235

770   Nie, D., Shen, F., Wang, J., Ma, X., Li, Z., Ge, P., Ou, Y., Jiang, Y., Chen, Meijuan,

771   Chen, Mindong, Wang, T., Ge, X., 2021. Changes of air quality and its

772   associated health and economic burden in 31 provincial capital cities in China

773   during COVID-19 pandemic. Atmos Res 249, 105328.

774   https://doi.org/10.1016/j.atmosres.2020.105328

775   Peng, J., Hu, M., Guo, S., Du, Z., Zheng, Jing, Shang, D., Levy Zamora, M., Zeng, L.,

776   Shao, M., Wu, Y.-S., Zheng, Jun, Wang, Y., Glen, C.R., Collins, D.R., Molina,

777   M.J., Zhang, R., 2016. Markedly enhanced absorption and direct radiative

778   forcing of black carbon under polluted urban environments. Proceedings of the

779   National Academy of Sciences 113, 4266–4271.

780   https://doi.org/10.1073/pnas.1602310113

781   Polissar, A.V., Hopke, P.K., Paatero, P., Kaufmann, Y.J., Hall, D.K., Bodhaine, B.A.,

782   Dutton, E.G., Harris, J.M., 1999. The aerosol at Barrow, Alaska: long-term

trends and source locations. Atmospheric Environment 33, 2441–2458. https://doi.org/10.1016/S1352-2310(98)00423-3

Qin, M., Hu, A., Mao, J., Li, X., Sheng, L., Sun, J., Li, J., Wang, X., Zhang, Y., Hu, J., 2021. PM2.5 and O3 relationships affected by the atmospheric oxidizing capacity in the Yangtze River Delta, China. Science of The Total Environment 152268. https://doi.org/10.1016/j.scitotenv.2021.152268

Ramanathan, V., Carmichael, G., 2008. Global and regional climate changes due to black carbon. Nature Geoscience 1, 221–227. https://doi.org/10.1038/ngeo156

Sedlacek, A.J., Lewis, E.R., Onasch, T.B., Zuidema, P., Redemann, J., Jaffe, D., Kleinman, L.I., 2022. Using the Black Carbon Particle Mixing State to Characterize the Lifecycle of Biomass Burning Aerosols. Environ. Sci. Technol. 56, 14315–14325. https://doi.org/10.1021/acs.est.2c03851

Silva, P.J., Liu, D.-Y., Noble, C.A., Prather, K.A., 1999. Size and Chemical Characterization of Individual Particles Resulting from Biomass Burning of Local Southern California Species. Environ. Sci. Technol. 33, 3068–3076. https://doi.org/10.1021/es980544p

Song, X.-H., Hopke, P.K., Fergenson, D.P., Prather, K.A., 1999. Classification of Single Particles Analyzed by ATOFMS Using an Artificial Neural Network, ART-2A. Anal. Chem. 71, 860–865. https://doi.org/10.1021/ac9809682

Steinfeld, J.I., 1998. Atmospheric Chemistry and Physics: From Air Pollution to Climate Change. Environment: Science and Policy for Sustainable Development 40, 26–26. https://doi.org/10.1080/00139157.1999.10544295

Sulaymon, I.D., Zhang, Yuanxun, Hopke, P.K., Hu, J., Zhang, Yang, Li, L., Mei, X., Gong, K., Shi, Z., Zhao, B., Zhao, F., 2021a. Persistent high PM2.5 pollution driven by unfavorable meteorological conditions during the COVID-19 lockdown period in the Beijing-Tianjin-Hebei region, China. Environmental Research 198, 111186. https://doi.org/10.1016/j.envres.2021.111186

Sulaymon, I.D., Zhang, Yuanxun, Hopke, P.K., Zhang, Yang, Hua, J., Mei, X., 2021b. COVID-19 pandemic in Wuhan: Ambient air quality and the relationships between criteria air pollutants and meteorological variables before, during, and after lockdown. Atmospheric Research 250, 105362. https://doi.org/10.1016/j.atmosres.2020.105362

Sun, J., Sun, Y., Xie, C., Xu, Weiqi, Chen, C., Wang, Zhe, Li, L., Du, X., Huang, F., Li, Y., Li, Z., Pan, X., Ma, N., Xu, Wanyun, Fu, P., Wang, Zifa, 2022. The chemical composition and mixing state of BC-containing particles and the implications on light absorption enhancement. Atmos. Chem. Phys. 22, 7619–7630. https://doi.org/10.5194/acp-22-7619-2022

Sun, J., Wang, Zhe, Zhou, W., Xie, C., Wu, C., Chen, C., Han, T., Wang, Q., Li, Z., Li, J., Fu, P., Wang, Zifa, Sun, Y., 2021. Measurement report: Long-term changes in black carbon and aerosol optical properties from 2012 to 2020 in Beijing, China (preprint). Aerosols/Field Measurements/Troposphere/Physics (physical properties and processes). https://doi.org/10.5194/acp-2021-637

825 Sun, Y., Du, W., Fu, P., Wang, Q., Li, J., Ge, X., Zhang, Q., Zhu, C., Ren, L., Xu, W.,
826   Zhao, J., Han, T., Worsnop, D.R., Wang, Z., 2016. Primary and secondary
827   aerosols in Beijing in winter: sources, variations and processes. Atmos. Chem.
828   Phys.

829 Sun, Y., Lei, L., Zhou, W., Chen, C., He, Y., Sun, J., Li, Z., Xu, W., Wang, Q., Ji, D., Fu,
830   P., Wang, Z., Worsnop, D.R., 2020. A chemical cocktail during the COVID-19
831   outbreak in Beijing, China: Insights from six-year aerosol particle composition
832   measurements during the Chinese New Year holiday. Science of The Total
833   Environment 742, 140739. https://doi.org/10.1016/j.scitotenv.2020.140739

834 Surdu, M., Lamkaddam, H., Wang, D.S., Bell, D.M., Xiao, M., Lee, C.P., Li, D.,
835   Caudillo, L., Marie, G., Scholz, W., Wang, M., Lopez, B., Piedehierro, A.A.,
836   Ataei, F., Baalbaki, R., Bertozzi, B., Bogert, P., Brasseur, Z., Dada, L., Duplissy,
837   J., Finkenzeller, H., He, X.-C., Höhler, K., Korhonen, K., Krechmer, J.E.,
838   Lehtipalo, K., Mahfouz, N.G.A., Manninen, H.E., Marten, R., Massabò, D.,
839   Mauldin, R., Petäjä, T., Pfeifer, J., Philippov, M., Rörup, B., Simon, M., Shen,
840   J., Umo, N.S., Vogel, F., Weber, S.K., Zauner-Wieczorek, M., Volkamer, R.,
841   Saathoff, H., Möhler, O., Kirkby, J., Worsnop, D.R., Kulmala, M., Stratmann,
842   F., Hansel, A., Curtius, J., Welti, A., Riva, M., Donahue, N.M., Baltensperger,
843   U., El Haddad, I., 2023. Molecular Understanding of the Enhancement in
844   Organic Aerosol Mass at High Relative Humidity. Environ Sci Technol 57,
845   2297–2309. https://doi.org/10.1021/acs.est.2c04587

846 Taylor, J.W., Allan, J.D., Allen, G., Coe, H., Williams, P.I., Flynn, M.J., Le Breton, M.,
847   Muller, J.B.A., Percival, C.J., Oram, D., Forster, G., Lee, J.D., Rickard, A.R.,
848   Parrington, M., Palmer, P.I., 2014. Size-dependent wet removal of black carbon
849   in Canadian biomass burning plumes. Atmospheric Chemistry and Physics 14,
850   13755–13771. https://doi.org/10.5194/acp-14-13755-2014

851 Wang, H., Miao, Q., Shen, L., Yang, Q., Wu, Y., Wei, H., 2021. Air pollutant variations
852   in Suzhou during the 2019 novel coronavirus (COVID-19) lockdown of 2020:
853   High time-resolution measurements of aerosol chemical compositions and
854   source   apportionment.   Environmental   Pollution   271,   116298.
855   https://doi.org/10.1016/j.envpol.2020.116298

856 Wang, J., Ge, X., Sonya, C., Ye, J., Lei, Y., Chen, M., Zhang, Q., 2022. Influence of
857   regional emission controls on the chemical composition, sources, and size
858   distributions of submicron aerosols: Insights from the 2014 Nanjing Youth
859   Olympic Games. Science of The Total Environment 807, 150869.
860   https://doi.org/10.1016/j.scitotenv.2021.150869

861 Wang, J., Liu, D., Ge, X., Wu, Y., Shen, F., Chen, M., Zhao, J., Xie, C., Wang, Q., Xu,
862   W., Zhang, J., Hu, J., Allan, J., Joshi, R., Fu, P., Coe, H., Sun, Y., 2019.
863   Characterization of black carbon-containing fine particles in Beijing during
864   wintertime. Atmos. Chem. Phys. 19, 447–458. https://doi.org/10.5194/acp-19-
865   447-2019

866 Wang, Pengfei, Chen, K., Zhu, S., Wang, Peng, Zhang, H., 2020. Severe air pollution

867   events not avoided by reduced anthropogenic activities during COVID-19
868   outbreak. Resources, Conservation and Recycling 158, 104814.
869   https://doi.org/10.1016/j.resconrec.2020.104814

870 Wang, Q., Liu, S., Zhou, Y., Cao, J., Han, Y., Ni, H., Zhang, N., Huang, R., 2015.
871   Characteristics of Black Carbon Aerosol during the Chinese Lunar Year and
872   Weekdays in Xi'an, China. Atmosphere 6, 195–208.
873   https://doi.org/10.3390/atmos6020195

874 Wang, S., Zhao, M., Xing, J., Wu, Y., Zhou, Y., Lei, Y., He, K., Fu, L., Hao, J., 2010.
875   Quantifying the Air Pollutants Emission Reduction during the 2008 Olympic
876   Games in Beijing. Environ. Sci. Technol. 44, 2490–2496.
877   https://doi.org/10.1021/es9028167

878 Wang, Y., Zhu, S., Ma, J., Shen, J., Wang, Pengfei, Wang, Peng, Zhang, H., 2021.
879   Enhanced atmospheric oxidation capacity and associated ozone increases
880   during COVID-19 lockdown in the Yangtze River Delta. Science of The Total
881   Environment 768, 144796. https://doi.org/10.1016/j.scitotenv.2020.144796

882 Wang, Y.Q., 2014. MeteoInfo: GIS software for meteorological data visualization and
883   analysis. Meteorological Applications 21, 360–368.
884   https://doi.org/10.1002/met.1345

885 Wang, Y.Q., Zhang, X.Y., Draxler, R.R., 2009. TrajStat: GIS-based software that uses
886   various trajectory statistical analysis methods to identify potential sources from
887   long-term air pollution measurement data. Environmental Modelling &
888   Software 24, 938–939. https://doi.org/10.1016/j.envsoft.2009.01.004

889 WHO global air quality guidelines: Particulate matter (PM2.5 and PM10), ozone,
890   nitrogen dioxide, sulfur dioxide and carbon monoxide, 2021. , WHO Guidelines
891   Approved by the Guidelines Review Committee. World Health Organization,
892   Geneva.

893 Xie, C., He, Y., Lei, L., Zhou, W., Liu, J., Wang, Q., Xu, W., Qiu, Y., Zhao, J., Sun, J.,
894   Li, L., Li, M., Zhou, Z., Fu, P., Wang, Z., Sun, Y., 2020. Contrasting mixing
895   state of black carbon-containing particles in summer and winter in Beijing.
896   Environmental Pollution 263, 114455.
897   https://doi.org/10.1016/j.envpol.2020.114455

898 Xu, J., Ge, X., Zhang, X., Zhao, W., Zhang, R., Zhang, Y., 2020. COVID-19 Impact on
899   the Concentration and Composition of Submicron Particulate Matter in a
900   Typical City of Northwest China. Geophysical Research Letters 47,
901   e2020GL089035. https://doi.org/10.1029/2020GL089035

902 Yang, J., Ma, S., Gao, B., Li, X., Zhang, Y., Cai, J., Li, M., Yao, L., Huang, B., Zheng,
903   M., 2017. Single particle mass spectral signatures from vehicle exhaust particles
904   and the source apportionment of on-line PM2.5 by single particle aerosol mass
905   spectrometry. Science of The Total Environment 593–594, 310–318.
906   https://doi.org/10.1016/j.scitotenv.2017.03.099

907 Zhang, G., Fu, Y., Peng, X., Sun, W., Shi, Z., Song, W., Hu, W., Chen, D., Lian, X., Li,
908   L., Tang, M., Wang, X., Bi, X., 2021. Black Carbon Involved Photochemistry

Enhances the Formation of Sulfate in the Ambient Atmosphere: Evidence From In Situ Individual Particle Investigation. Geophys Res Atmos 126. https://doi.org/10.1029/2021JD035226

Zhang, J., Li, H., Chen, L., Huang, X., Zhang, W., Zhao, R., 2022. Particle composition, sources and evolution during the COVID-19 lockdown period in Chengdu, southwest China: Insights from single particle aerosol mass spectrometer data. Atmospheric Environment 268, 118844. https://doi.org/10.1016/j.atmosenv.2021.118844

Zhang, J., Yuan, Q., Liu, L., Wang, Y., Zhang, Y., Xu, L., Pang, Y., Zhu, Y., Niu, H., Shao, L., Yang, S., Liu, H., Pan, X., Shi, Z., Hu, M., Fu, P., Li, W., 2021. Trans-Regional Transport of Haze Particles From the North China Plain to Yangtze River Delta During Winter. JGR Atmospheres 126. https://doi.org/10.1029/2020JD033778

Zhang, K., Liu, Z., Zhang, X., Li, Q., Jensen, A., Tan, W., Huang, L., Wang, Y., de Gouw, J., Li, L., 2022. Insights into the significant increase in ozone during COVID-19 in a typical urban city of China. Atmos. Chem. Phys. 22, 4853–4866. https://doi.org/10.5194/acp-22-4853-2022

Zhang, Y., Liu, X., Zhang, L., Tang, A., Goulding, K., Collett, J.L., 2021. Evolution of secondary inorganic aerosols amidst improving PM2.5 air quality in the North China plain. Environmental Pollution 281, 117027. https://doi.org/10.1016/j.envpol.2021.117027

Zhang Y., Wang X., Chen H., Yang X., Chen J., Alien J.O., 2009. Source Apportionment Of Lead-containing Aerosol Particles In Shanghai Using Single Particle Mass Spectrometry. Chemosphere 74, 501–507.

Zhang, Y., Yuan, Q., Huang, D., Kong, S., Zhang, J., Wang, X., Lu, C., Shi, Z., Zhang, X., Sun, Y., Wang, Z., Shao, L., Zhu, J., Li, W., 2018. Direct Observations of Fine Primary Particles From Residential Coal Burning: Insights Into Their Morphology, Composition, and Hygroscopicity. Journal of Geophysical Research: Atmospheres 123, 12,964-12,979. https://doi.org/10.1029/2018JD028988

Zhang, Z., Li, H., Ho, W., Cui, L., Men, Q., Cao, L., Zhang, Y., Wang, J., Huang, C., Lee, S., Huang, Y., Chen, M., Ge, X., 2024. Critical Roles of Surface-Enhanced Heterogeneous Oxidation of SO2 in Haze Chemistry: Review of Extended Pathways for Complex Air Pollution. Curr Pollution Rep. https://doi.org/10.1007/s40726-023-00287-2

Zhou, H., Liu, T., Sun, B., Tian, Y., Zhou, X., Hao, F., Chun, X., Wan, Z., Liu, P., Wang, J., Du, D., 2022. Chemical characteristics and sources of PM2.5 in Hohhot, a semi-arid city in northern China: insight from the COVID-19 lockdown. Atmos. Chem. Phys. 14.

Zhou, X., Gao, J., Wang, T., Wu, W., Wang, W., 2009. Measurement of black carbon aerosols near two Chinese megacities and the implications for improving emission inventories. Atmospheric Environment 43, 3918–3924.

951   https://doi.org/10.1016/j.atmosenv.2009.04.062

952 Zhou, Y., Wu, Y., Yang, L., Fu, L., He, K., Wang, S., Hao, J., Chen, J., Li, C., 2010. The
953   impact of transportation control measures on emission reductions during the
954   2008 Olympic Games in Beijing, China. Atmospheric Environment 44, 285–
955   293. https://doi.org/10.1016/j.atmosenv.2009.10.040

956 Zhu, X., Hu, B., Xin, J., Wang, L., Münkel, C., Mao, G., Wang, Y., 2015. Impact of
957   emission controls on air quality in Beijing during APEC 2014: Lidar ceilometer
958   observations. ATMOSPHERIC CHEMISTRY AND PHYSICS 15, 12667–
959   12680. https://doi.org/10.5194/acp-15-12667-2015

960

961
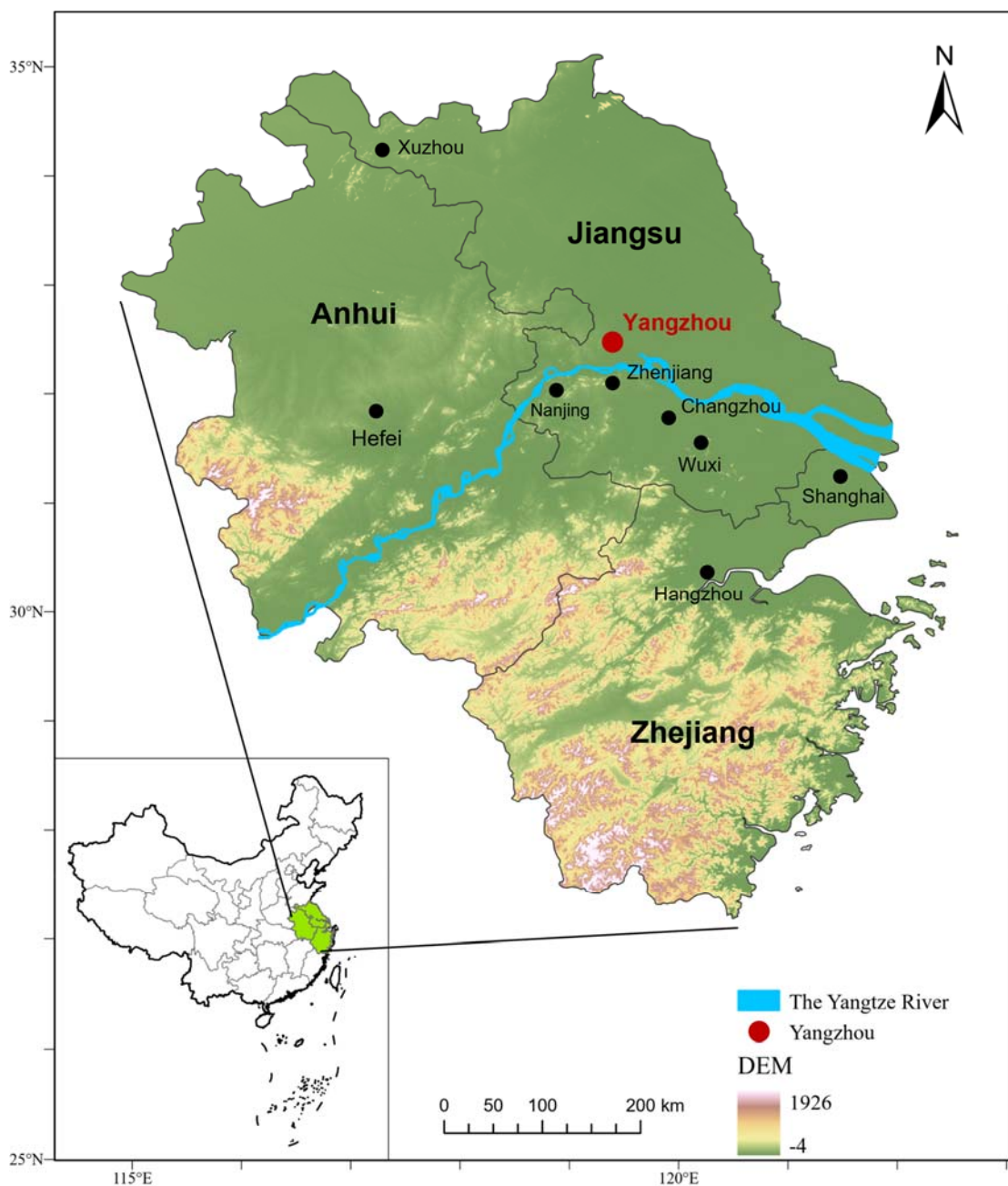
963 **Figure 1.** Geographical overview of the Yangtze River Delta (YRD) Region in China,

964 depicting the major cities within the YRD and the sampling site located in Yangzhou.
965 The color gradient from green to white indicates varying altitudes across the region
966 (Maps were generated by using ArcGIS Pro).
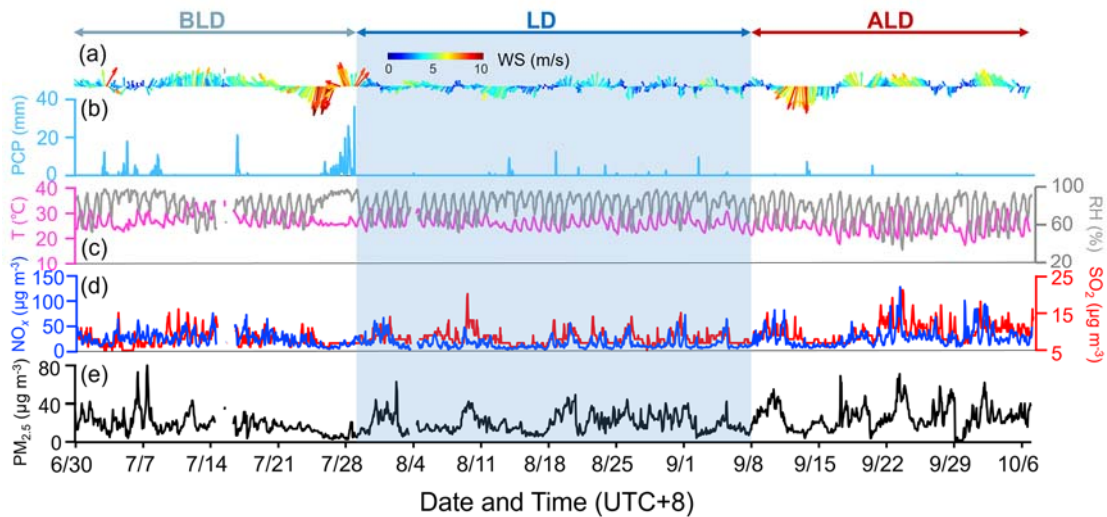
967

968 **Figure 2.** Temporal variations of **(a)** wind direction (WD) and wind speed (WS), **(b)**
969 precipitation (PCP), **(c)** temperature (T) and relative humidity (RH), **(d)** concentrations
970 of NO$_x$ and SO$_2$, and **(e)** mass loading of PM$_{2.5}$. The grey, blue, and red arrow ranges
971 denote the periods before lockdown (BLD), during lockdown (LD), and after lockdown
972 (ALD).
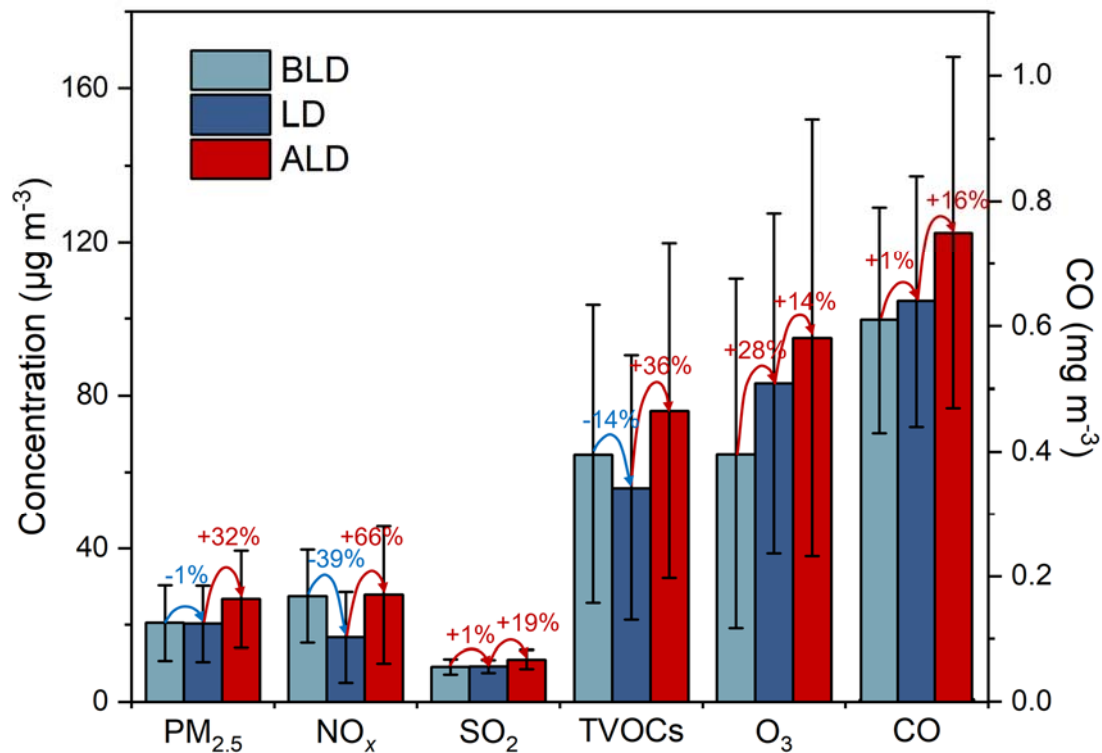
973

974 **Figure 3.** Ground-based observations of PM$_{2.5}$, NO$_x$, SO$_2$, O$_3$, CO, and TVOC

975 concentrations in Yangzhou. The figure compares the averages during the BLD (grey),
976 LD (blue), and ALD (red) periods. Error bars indicate SDs over different lockdown
977 periods.
978
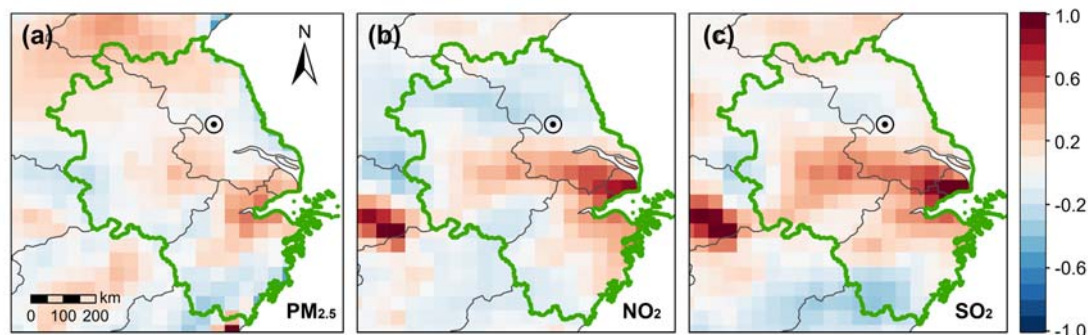
979

980 **Figure 4.** The fractional changes (i.e., (LD – BLD)/BLD) of **(a)** PM$_{2.5}$, **(b)** NO$_2$, and **(c)**
981 SO$_2$ between BLD and LD periods based on spaceborne measurement. The circle
982 symbols in the maps indicate the location of Yangzhou, and the green region represents
983 the YRD.
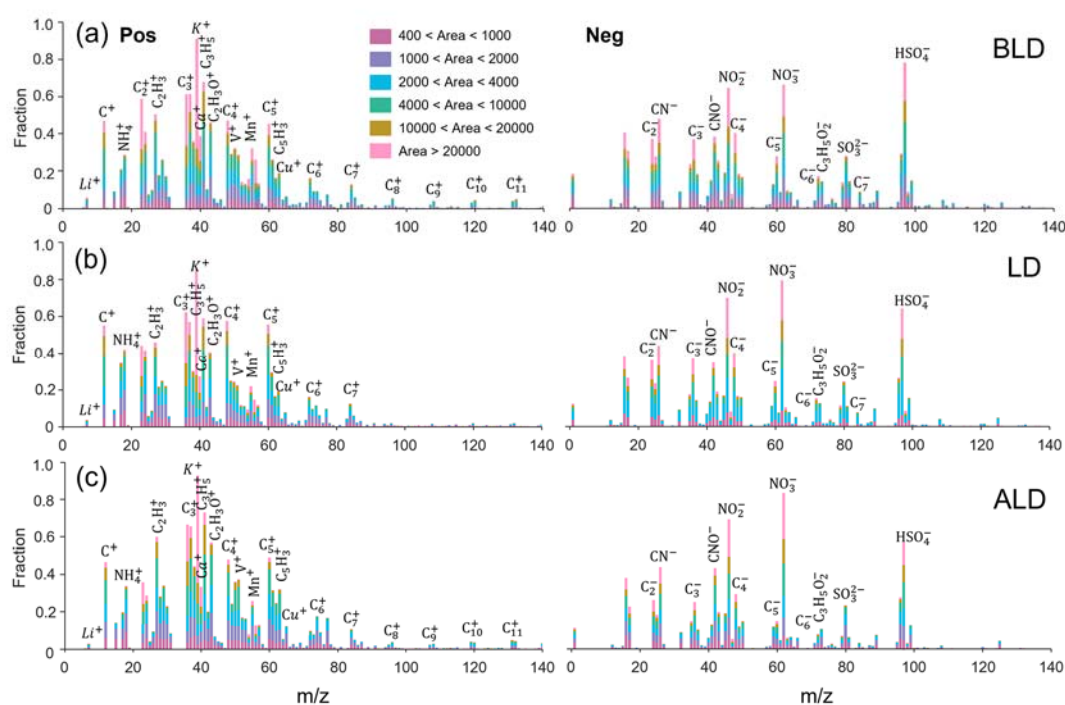
984

985 **Figure 5.** The average positive and negative mass spectra of BCc **(a)** before the
986 lockdown period (BLD), **(b)** during the lockdown period (LD), and **(c)** after the
987 lockdown period (ALD).
988
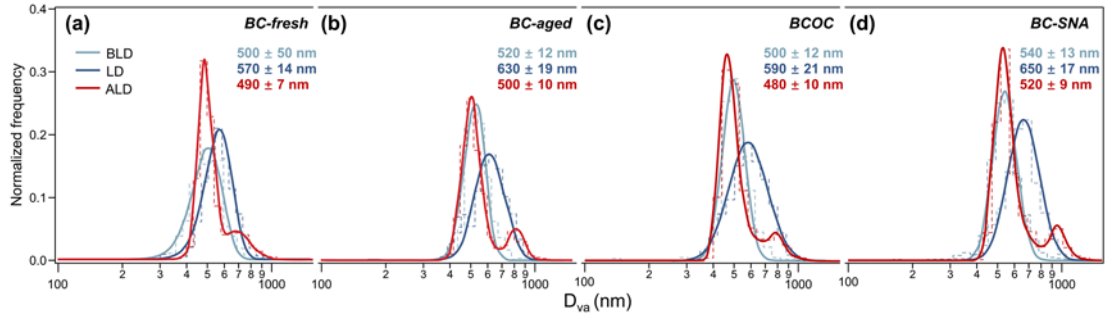
989

990 **Figure 6.** Size distribution of different types of BCc during different periods in
991 Yangzhou. **(a)** BC-fresh particles, **(b)** BC-aged particles, **(c)** BCOC particles, and **(d)**
992 BC-SNA particles. The Log-normal distribution was used to fit the unimodal size
993 distribution, and the Lorentz distribution was used to fit the bimodal size distribution.
994 The corresponding mode sizes (with the standard deviations) are also shown.

995
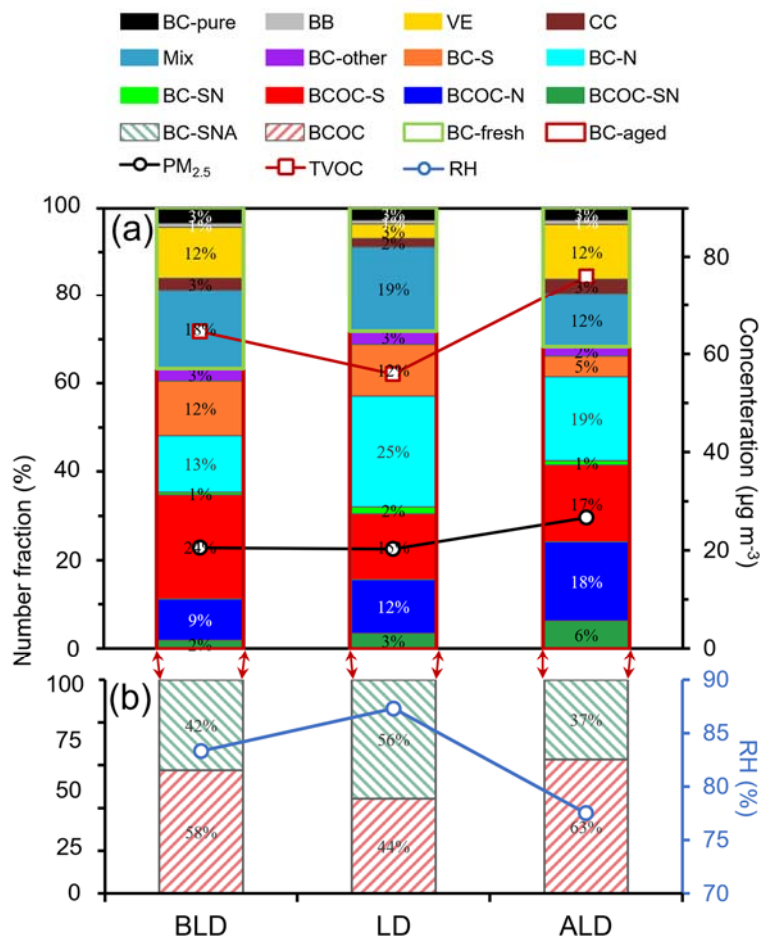
996

997 **Figure 7.** Number fractions of BCc. **(a)** The number fractions of different BCc along
998 with the concentrations of $PM_{2.5}$ and total volatile organic compounds (TVOC). **(b)** The

999 number fractions of different types of BC-aged particles along with relative humidity
1000 (RH).
1001
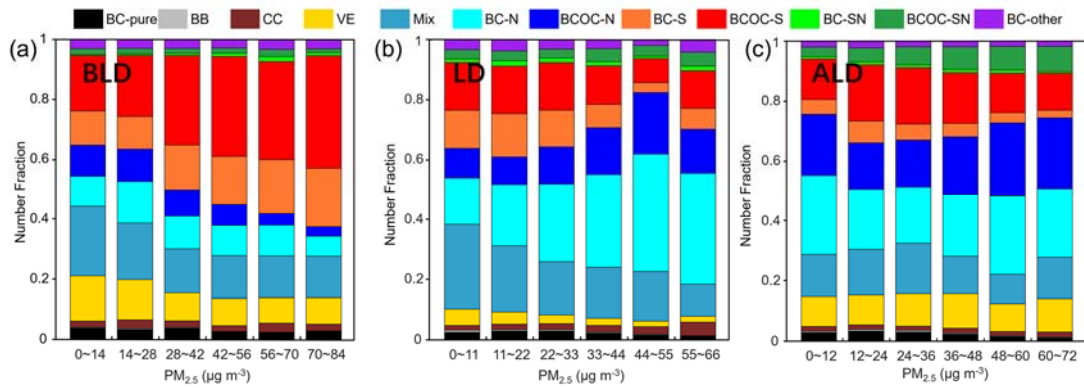
1002

Figure 8. Variations of number fractions of BCc particle types with PM$_{2.5}$ mass
concentrations during **(a)** the BLD period, **(b)** LD, and **(c)** the ALD period.
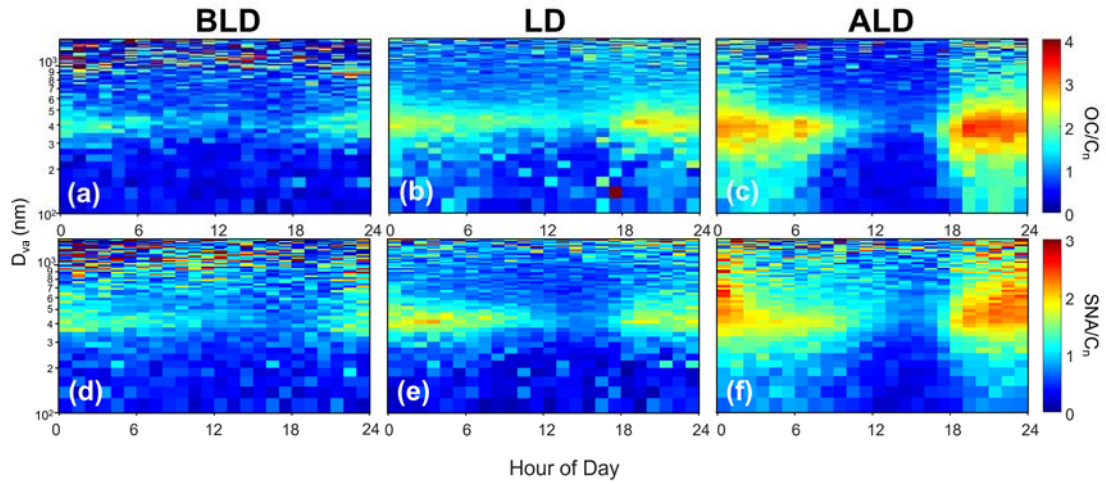
1005

Figure 9. Diurnal variations of the ratios of OC/Cn and SNA/Cn with a size distribution
of BCc during **(a, d)** BLD, **(b, e)** LD, and **(c, f)** ALD.
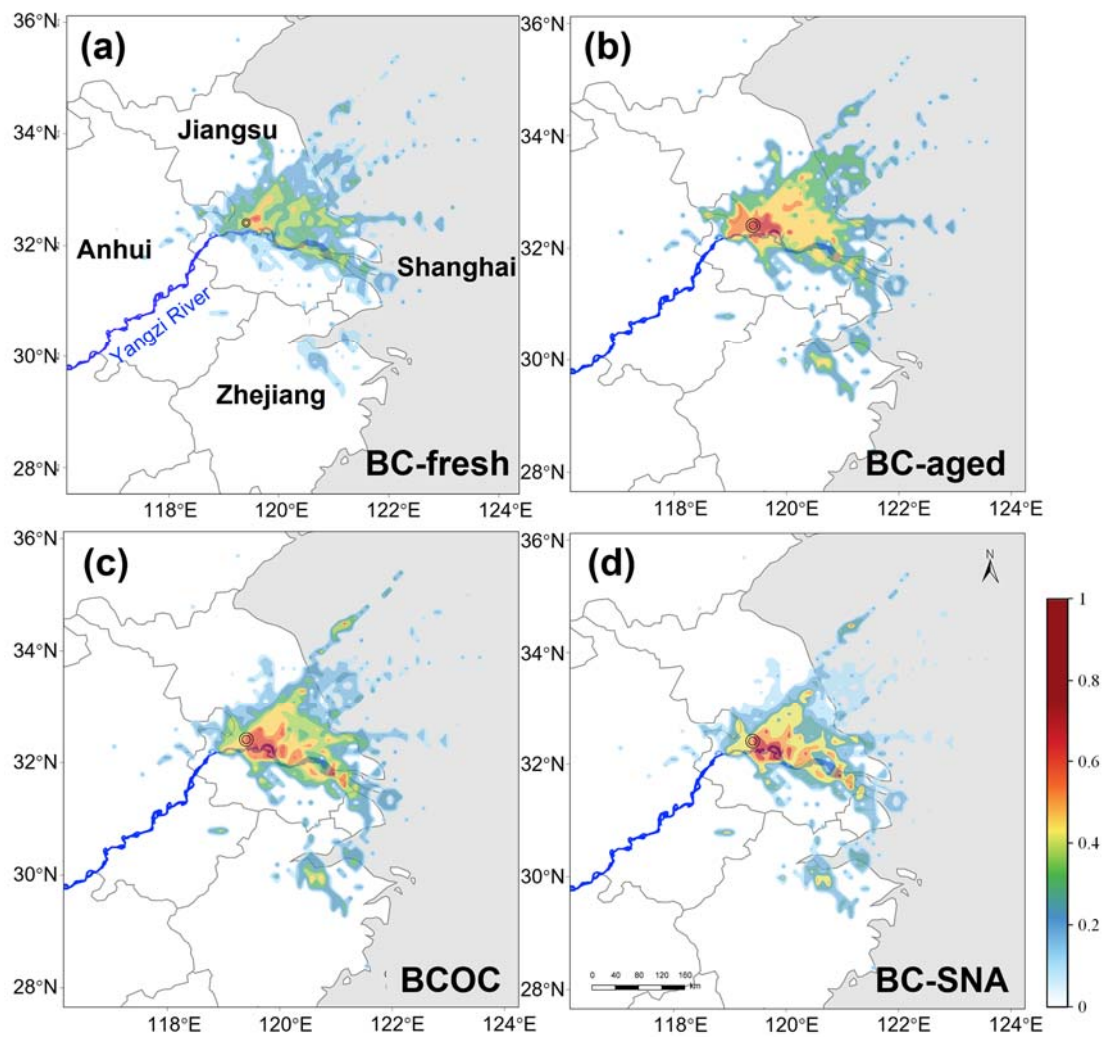
1008

1009 **Figure 10.** The PSCF maps for different BCc during LD. **(a)** BC-fresh. **(b)** BC-aged.
1010 **(c)** BCOC. **(d)** BC-SNA.
1011